Proceedings of AJK2011-FED
The ASME-JSME-KSME Joint Fluids Engineering Conference 2011 (AJK2011-FED)
July 24 - 29, 2011, Hamamatsu, Japan

AJK2011-16010

EFFECT OF REYNOLDS NUMBER ON THE TURBULENT FLOW STRUCTURE IN THE NEAR-WALL REGION OF AN IMPINGING ROUND JET

Khaled J. Hammad
Dantec Dynamics Inc.
Holtsville, NY, USA

Ivana Milanovic
University of Hartford
West Hartford, CT, USA

ABSTRACT

Time-Resolved Particle Image Velocimetry was used to study the effect of the Reynolds number on the turbulent flow structure of a submerged water jet impinging normally on a smooth and flat surface. A fully developed turbulent jet and a semi-confined flow configuration ensured properly characterized boundary conditions allowing for straightforward assessment of turbulence models and numerical schemes. The Reynolds number based on jet mean exit velocity was 5,000, 10,030 and 15,050 while the pipe-to-plate separation distance was fixed at two diameters. Turbulent velocity fields are presented using Reynolds decomposition into mean and fluctuating components while Proper Orthogonal Decomposition (POD) analysis identified the most energetic coherent structures in the stagnation and wall-jet regions.

NOMENCLATURE

D	Pipe internal diameter (m)
H	Pipe-to-plate separation distance (m)
L	Pipe length (m)
Re	Reynolds number ($U_b D/\nu$)
U_c	Mean centerline velocity at the pipe exit (m/s)
U_b	Pipe bulk velocity (m/s)
u, v	Normalized mean axial and radial velocities $(U/U_c, V/U_c)$
u_i, v_i	Instantaneous axial and radial velocity (m/s)
u', v'	Normalized axial and radial RMS velocities

Greek Symbols

ν	Kinematic viscosity of jet fluid (m^2/s)

Subscripts

b	Bulk
c	Centerline
j	Jet
p	Pipe
r	Radial
x	Axial

INTRODUCTION

Jet impingement is used in many technologically important applications such as cooling/heating, drying, mixing and chemical vapor deposition (CVD) processes. Figure 1 illustrates three distinct regions that may be observed in an impinging jet: (1) the 'free' jet, where the flow does not feel the presence of the wall and the surrounding fluid is entrained into the jet; (2) the impingement or stagnation region, where the wall imposes pressure gradients changing the direction of streamlines from the axial to the radial, and (3) the wall-jet region where a complete deflection of the jet is accomplished while the region is characterized by strong shear and velocity fluctuation levels much higher than in an ordinary boundary layer.

Impinging jets have been extensively studied with focus on the flow, heat/mass transfer characteristics, and turbulence modeling. Comprehensive reviews of impinging jet research are provided by Martin [1], Downs *et al.* [2], Jambunathan *et al.* [3], Viskanta [4], Polat [5], Webb *et al.* [6] and Garimella [7]. Spatial topology of a round impinging jet issuing from a long pipe at a high Reynolds number was investigated in large eddy simulations (LES) of Hadziabdic and Hanjalic [8] at Re = 20,000 and separation distance H/D = 2 and in a snapshot Proper Orthogonal Decomposition (POD) study of Hammad and Milanovic [9] at Re = 16,000 with separation distances between 1 and 8D. The aforementioned works revealed interesting time and spatial dynamics of the vortical structures and their imprints on the wall.

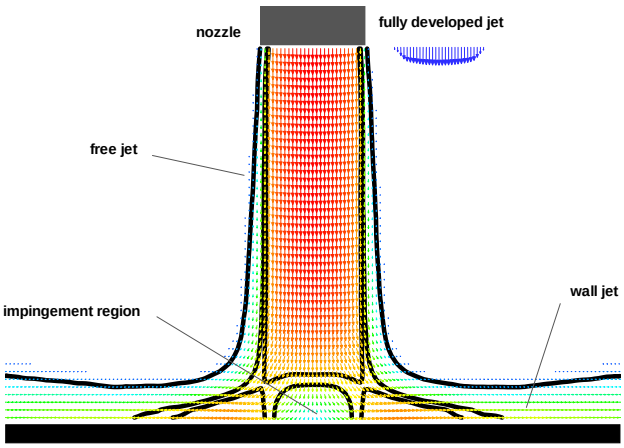

FIGURE 1. IMPINGING JET SCHEMATIC

Shear layer instability near the nozzle lip at moderate and high Reynolds numbers results in the formation of large vortical structures. This instability is controlled by the processes taking place at two different length scales: (1) the momentum thickness of the boundary layer at the nozzle lip, critical to the initial development of the shear layer, and (2) the jet diameter, D, which becomes important further downstream. Recent studies [8-9] highlighted the influence of vortical structures on flow and heat transfer characteristics and emphasized the need for further research focusing on jet-wall interactions. The present work used time-resolved PIV (TR-PIV) measurements to study the effect of the Reynolds number on the flow field resulting from a submerged water jet impinging normally on a smooth and flat surface. The selected flow configuration, inflow and boundary conditions allow for straightforward assessment of turbulence models and numerical schemes. Statistically averaged mean and RMS velocities are reported with emphasis on the near-wall region. POD analysis of the TR-PIV data was used to gain insight into the most energetic coherent structures of the turbulent flow field. The experimental setup and test procedure used in this investigation are presented below.

EXPERIMENTAL SETUP

Figure 2 illustrates the experimental setup for the PIV measurements. A closed-loop system is composed of the test section, pump, and the pipe mount. The rectangular and impingement plate are made of smooth finish, clear cast acrylic with the impingement plate diameter D_{plate} = 101.6 mm, thickness of 12.7 mm and tank height H_{tank} = 279.4 mm.

The jet was produced using a submerged vertical precision type 304 stainless steel tube placed on the cylinder centerline with an inner diameter D = 6.35 mm, length L = 711.2 mm and wall thickness 0.381 mm. The length-to-diameter ratio of the tube, L/D = 112, assured fully developed turbulent flow conditions at the outlet. The resulting D_{plate}/D ratio is 16.

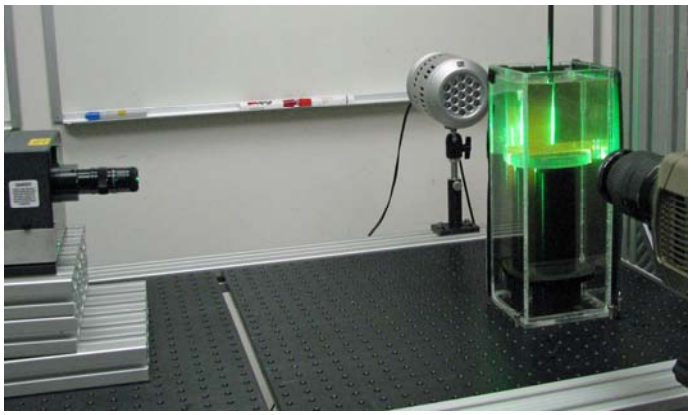

FIGURE 2. EXPERIMENTAL SETUP

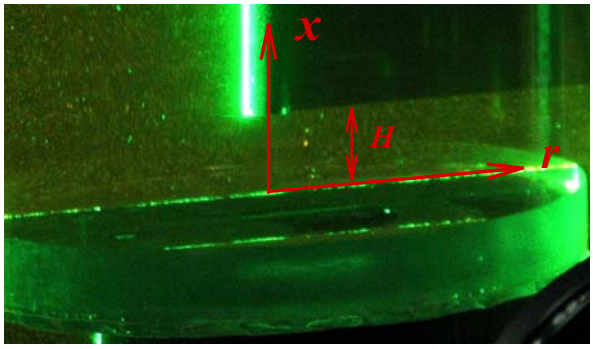

FIGURE 3. TEST SECTION AND COORDINATE SYSTEM

As shown in Fig. 2, after impinging the circular plate the flow leaves the test section through the bottom of the rectangular tank. As shown in Fig. 3, the separation distance between the pipe outlet and the cylindrical impingement plate is denoted by H. The origin of the cylindrical r,x coordinate system coincides with the stagnation point. The x-axis is pointing away from the impingement plate in the vertical direction. The r coordinate is measured along the bottom circular plate.

Measurements were performed at a fixed pipe-to-plate separation distance, H/D = 2. Volumetric flow rates of 1.827×10^{-5} m^3/s (0.29 GPM), 3.591×10^{-5} m^3/s (0.57 GPM) and 5.229×10^{-5} m^3/s (0.83 GPM) were used, resulting in pipe bulk velocity, U_b, of 0.58, 1.13 and 1.68 m/s, respectively. The kinematic viscosities of the working fluid, DI water at 34, 35 and 36°C, were 7.33×10^{-7}, 7.18×10^{-7} and 6.97×10^{-7} m^2/s. The Reynolds number, Re, based on jet mean exit velocity was 5,000, 10,030 and 15,050.

PIV SYSTEM AND DATA PROCESSING

A DANTEC DYNAMICS two-dimensional TR-PIV system was used to measure the flow field along each *rx* plane of interest. The system consisted of synchronization hardware for controlling the laser and camera, and software running on a Windows-based platform for data acquisition, management and post-analysis. The light source was a New-Wave Research Pegasus® dual-head, diode-pumped Nd:YLF laser system.

Each laser head had operating range between 1 and 10,000 pulses per second. When fired at 1 kHz, the resulting per-cavity energy at 527 nm is 10 mJ. A Phantom® v210, 1Mpx high-speed camera capable of taking more than 2,000 frames-per-second (fps) at full 1280 x 800 pixel resolution was used. The CMOS camera has an active pixel size of 20 microns with 8- and 12-bit pixel depth.

The Nd:YLF laser was fired at a frequency of 100 Hz, yielding 200 pulses of green (527-nm wavelength) 1.5 mm beams, each having a typical duration of about 180 ns. Light sheet forming optics mounted at the exit portal of the laser system generated a thin, focusable light sheet by means of a series of spherical and cylindrical lenses. A vertical divergent light sheet was used to illuminate the full extent of the measurement region within the cylindrical tank. The vertical light sheet was aligned to pass through the center of the pipe. The thickness of the light sheet at the imaging plane was 1 mm. The spatial location of the illumination system was fixed during all the tests. The CMOS camera was placed perpendicular to the laser sheet. The lens used was a Nikon Micro-Nikkor 105 mm.

To eliminate image contamination or saturation due to high intensity reflections near the metal surfaces, fluorescent polystyrene particles were used as the tracer. The particles fluoresced when illuminated by the green laser light. A high pass color filter was then used to discriminate particle fluorescence from surface reflections and other Mie-type of scattering. The average diameter of the fluorescent particles was 15 μm with the density of 1.05 g/cm^3. The latter value was close to the water density (0.994 g/cm^3); hence the particles were nearly neutrally buoyant in the measurement region.

For the present set of measurements, a high-accuracy multi-pass adaptive cross-correlation technique was used to evaluate the velocity field determined from each pair of particle images. A high sub-pixel accuracy independent of correlation peak shape was achieved and further minimized displacement estimate errors [10].

The final interrogation area, IA, was 16 × 16 pixels with 50% overlap in both the horizontal and vertical directions. An initial IA of 128 × 128 pixels was sequentially reduced to the final IA. A dynamic second-order accurate method was used to spatially offset the two IA's during each subsequent iteration cycle by the displacement calculated from previous steps. During each iteration cycle, checks on the correlation's signal-to-noise, as well as a local comparison of vector attributes with the median value of 3 × 3 neighbors were applied to validate and remove outliers. To remove spurious vectors, a minimum peak height ratio (between the 1st and 2nd peak) of 1.2 was selected, thereby enforcing more stringent conditions on peak identification for the subsequent determination of vectors.

Three thousand PIV realizations at a sampling rate of 100 Hz were obtained for all test cases and used to evaluate the mean and RMS flow field information presented here.

The focus of the current work was to investigate the flow structure close to the impingement region. Therefore, the results correspond to a 1*D* × 5*D* rectangular sub-region situated above the impingement wall. The final IA was 16 × 16 pixels for all test cases. Each obtained vector represented the spatial average over a 0.59 × 0.59 × 1 mm volume. Each obtained vector map corresponded to 21 vectors along the x direction and 110 along the r direction, a total of 2,310 vectors.

The pipe exit region was also analyzed to investigate the exit flow conditions 0.1*D* from the nozzle. The centerline axial velocity, U_c, was measured for all pipe-to-plate distances, and subsequently used to normalize reported flow field data. Measured U_c values were 0.90, 1.63 and 2.37 m/s for *Re* = 5,000, 10,030 and 15,050, respectively.

REYNOLDS DECOMPOSITION

The mean velocity is given by the following equation:

$$U = \frac{1}{N}\sum_{i=1}^{N} u_i \tag{1}$$

where u_i is measured instantaneous velocity and N is the number of PIV data sets. Both the radial and axial components of the mean velocity are calculated using Eq. (1). The fluctuating velocities are obtained after evaluating the mean velocity. Normal and shear Reynolds stresses are calculated using the following equations:

$$\overline{u'^2} = \frac{1}{N}\sum_{i=1}^{N}(u_i - U)^2$$
$$\overline{v'^2} = \frac{1}{N}\sum_{i=1}^{N}(v_i - V)^2 \tag{2}$$

Normalized axial, $u' = \sqrt{\overline{u'^2}}$, and radial, $v' = \sqrt{\overline{v'^2}}$, RMS velocity components are calculated and used for data presentation.

Figures 4 and 5 illustrate radial profiles of the mean and RMS velocities 0.1*D* away from the nozzle. While all velocities are normalized by the centerline axial velocity at the pipe exit, U_c, the axial and radial distances are normalized by the pipe diameter, *D*. The radial profiles of the mean axial (*u*), and radial (*v*) velocity, measured for *Re* = 5,000, 10,030 and 15,050, are given in Fig. 4. All shown velocity distributions obtained in the nozzle region, clearly demonstrate flow symmetry. Furthermore, normalized profiles collapse indicating fully developed pipe conditions. A comparison of axial profiles with expected fully developed pipe conditions as approximated by the empirical Power law, $u = (1 - 2r/D)^{1/n}$, is also given in

Fig. 4. Good correlation with experimental data is achieved for the 1/6th power low velocity profile (n = 6).

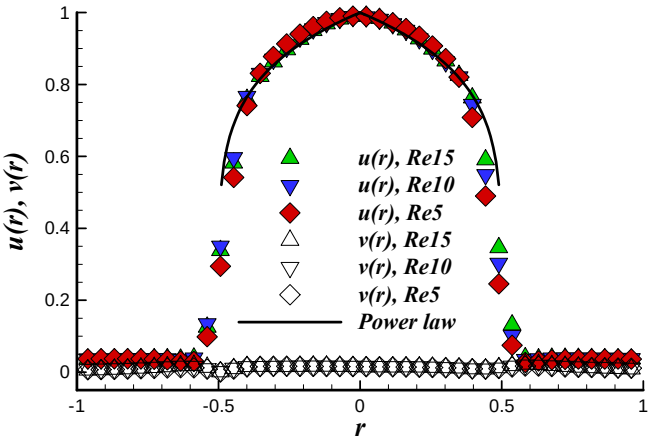

FIGURE 4. RADIAL TIME-AVERAGED VELOCITY PROFILES AT X = 0.1

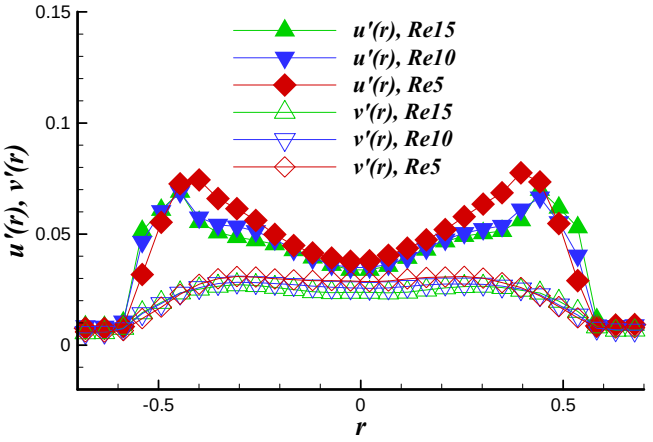

FIGURE 5. RADIAL RMS PROFILES AT X = 0.1

The radial profiles of RMS velocities, u' and v', are shown in Fig. 5. Close to the nozzle, v' values are generally low and do not vary much across the jet. However, u' distribution experiences substantial changes with two distinct peaks ($u' \approx 0.075, r \approx \pm 0.45D$) appearing at the edge of the jet due to the development of the turbulent shear layer. Noticeably different RMS value components confirm the anisotropy of the Reynolds normal stresses. Furthermore, variations across the jet core (region defined by $r = \pm 0.3$) are rather small with a local centerline turbulence intensity $u'_{CL} \approx 0.04$, or $u'_{CL}\left(U_c/U_b\right) \approx 0.05$. This is in good agreement with the expected value of about 4.7% for the Reynolds number of 15,050. The location $r = \pm 0.45$ can be considered the center of the annular shear layer where the velocity fluctuations are appreciably stronger than those found in the jet core.

The variation of the mean axial velocity, u_c, along the stagnation line, r = 0, is shown in Fig. 6. Curves for all three Reynolds numbers collapse. In the vicinity of x = 1, centerline velocity is dropping gradually, mainly due to the turbulent shear stresses. However, as the jet moves further downstream, x < 0.5, proximity to the plate results in a more rapid jet deceleration and centerline velocity decay.

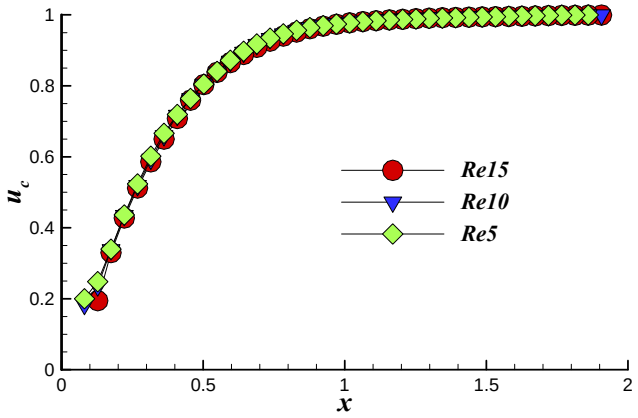

FIGURE 6. MEAN AXIAL VELOCITY DECAY ALONG STAGNATION LINE

Figures 7 and 8 provide a global view of the mean velocity field and RMS velocities in the impingement and the wall-jet regions for Reynolds numbers 15,050 and 5,000, respectively. Interaction of the fully developed turbulent jet with the non-stagnant ambient fluid results in radial spreading of the annular shear layer. As the jet approaches the plate, rapid flow deceleration and shear layer growth are observed for x < 0.5. The presence of a stagnation zone leads to an overall radial deflection of the incoming flow and the formation of a wall-jet. In the wall-jet region, mean velocity contours indicate strong gradients reflecting the flow undergoing a deflection accompanied by acceleration, followed by a radial spreading of the wall-jet and deceleration.

Significant radial RMS velocities are visible only in the wall-jet region, $1 < |r| < 3$. This is expected due to the axial nature of the flow in the 'free' jet. The impacted region is of approximately the same length and somewhat wider for lower Reynolds numbers. Axial RMS velocity in the jet shear layer is stronger than in the jet core or ambient fluid. The annular shear layer grows radially by entrainment. However, a complete inward penetration for this separation distance is not achieved here due to the short separation distance. Complete inward penetration of the jet shear layer, or lack of it, significantly impacts the characteristics of momentum and heat transfer rates in the impingement and the wall-jet regions.

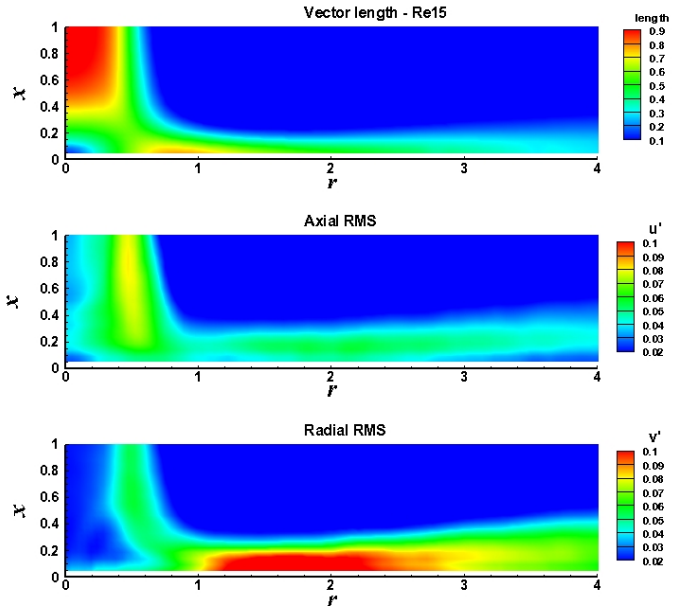

FIGURE 7. MEAN AND RMS VELOCITIES FOR RE = 15,050

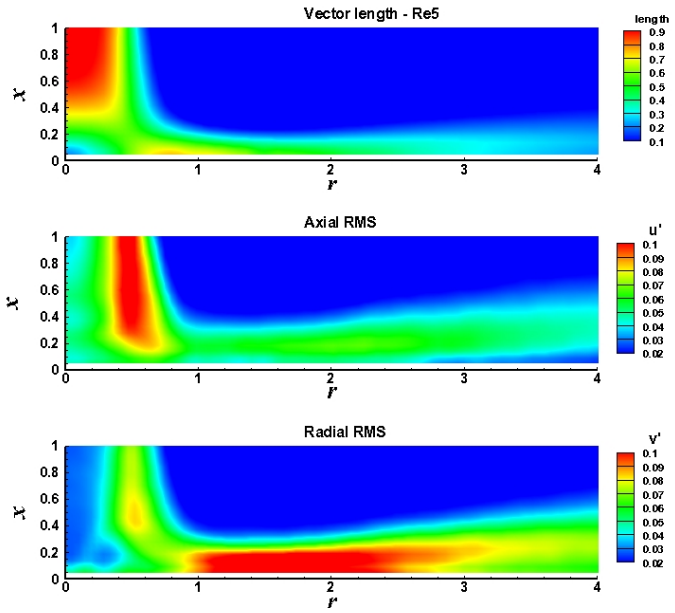

FIGURE 8. MEAN AND RMS VELOCITIES FOR RE = 5,000

POD APPROACH

Snapshot POD has been applied to 2D PIV data sets in a manner similar to that used by Meyer *et al.* [11]. The zero mode represents the mean velocity field. Fluctuating parts of velocity components for the *N* snapshots and *M* positions are arranged as follows:

$$\boldsymbol{U}=\begin{bmatrix}\boldsymbol{u}^1 & \boldsymbol{u}^2 & \dots & \boldsymbol{u}^{\mathrm{N}}\end{bmatrix}=\begin{bmatrix} u_1^1 & u_1^2 & \cdots & u_1^N \\ \vdots & \vdots & \vdots & \vdots \\ u_{\mathrm{M}}^1 & u_{\mathrm{M}}^2 & \cdots & u_{\mathrm{M}}^N \\ v_1^1 & v_1^2 & \dots & v_1^{\mathrm{N}} \\ \vdots & \vdots & \vdots & \vdots \\ v_{\mathrm{M}}^1 & v_{\mathrm{M}}^1 & \cdots & v_{\mathrm{M}}^1 \end{bmatrix} \tag{3}$$

The autocovariance matrix is created:

$$\tilde{\boldsymbol{C}}=\boldsymbol{U}^{\boldsymbol{T}}\boldsymbol{U} \tag{4}$$

And the eigenvalue problem is solved:

$$\tilde{\boldsymbol{C}}\boldsymbol{A}^i=\lambda^i\boldsymbol{A}^i \tag{5}$$

The solutions are arranged:

$$\boldsymbol{\lambda}_1>\boldsymbol{\lambda}_2>\ldots>\boldsymbol{\lambda}_N=0 \tag{6}$$

The eigenvalue corresponding to a spatial mode, λ_n, represents the fraction of turbulent kinetic energy associated with the mode.

POD spatial modes are now found:

$$\boldsymbol{\phi}^i=\frac{\sum_{n=1}^{N}A_n^i\boldsymbol{u}^n}{\left\|\sum_{n=1}^{N}A_n^i\boldsymbol{u}^n\right\|},i=1,....N \tag{7}$$

With POD modes arranged as:

$$\boldsymbol{\psi}=\begin{bmatrix}\boldsymbol{\phi}^1 & \boldsymbol{\phi}^2 & \dots & \boldsymbol{\phi}^N\end{bmatrix} \tag{8}$$

POD coefficients a_i can be found for the snapshot *n* as:

$$a_i=\boldsymbol{\phi}^i\boldsymbol{u}^n \tag{9}$$

$$a^n=\boldsymbol{\Psi}^{\boldsymbol{T}}\boldsymbol{u}^n \tag{10}$$

A snapshot (fluctuating part) can be reconstructed as:

$$\boldsymbol{u}^n=\sum_{i=1}^{N}a_i^n\boldsymbol{\phi}^i=\boldsymbol{\Psi}\boldsymbol{a}^n \tag{11}$$

Coherent structures can carry a substantial percentage of the total turbulent energy. A POD mode represents a coherent structure only if it contains a dominant percentage of energy. POD does not require any prior information on the flow and captures the most energetic components with just a few modes. It is used both as an advanced processing method to reveal the main energetic features by eliminating the low energy motions and as a means to construct low-dimensional dynamical models of coherent structures.

Turbulent energy distribution for the first 1,000 modes of each configuration is presented in Fig. 9. The rate of decay of the POD spectrum is an indication of the complexity of the flow. Flatter spectrum curves suggest a more complex flow where a larger number of modes contribute significantly to the turbulent energy.

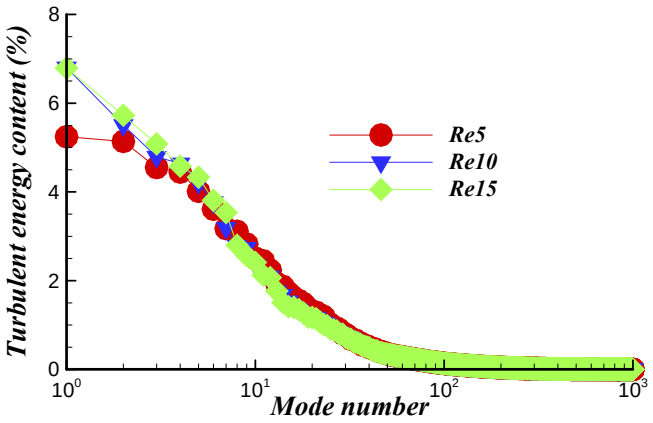

FIGURE 9. POD MODAL ENERGY DISTRIBUTION

The energy content of the ten dominant POD modes is listed in Table 1. POD modes 1-10 contain 38.63%, 40.78% and 41.62% of turbulent energy in the cases *Re* = 5,000, 10,030, and 15,050, respectively. The overall modal distribution is almost identical for *Re* = 10,030, and 15,050. The most significant POD mode, number one, in the case of *Re* = 5,000, displays a substantially lower energy content compared to those of *Re* = 10,030 and 15,050.

TABLE 1. MODAL ENERGY DISTRIBUTION FOR MODES 1-10

Re	*5,000*	*10,030*	*15,050*
Mode			
1	5.25%	6.80%	6.79%
2	5.14%	5.51%	5.73%
3	4.55%	4.79%	5.08%
4	4.45%	4.64%	4.58%
5	4.01%	4.20%	4.33%
6	3.61%	3.77%	3.81%
7	3.17%	3.19%	3.53%
8	3.11%	2.78%	2.80%
9	2.83%	2.74%	2.56%
10	2.51%	2.36%	2.41%
1-10	**38.63%**	**40.78%**	**41.62%**

The spatial flow characteristics of POD modes 1-10 are shown in Figs. 10 and 11 for Reynolds numbers of 5,000 and 15,050, respectively. The selected modes represent flow structures that contain substantial turbulent energy, 38.63% and 41.62%, as indicated in Table 1. For the given separation distance, *H/D* = 2, large scale flow structures are mainly present within the jet shear layer and above the impingement wall, outside of the stagnation region, $r > 0.5$.

The POD modes reveal the existence of vortical structures, developing in the mixing region, that stretch and acquire a strong radial component when they approach the impingement plate. The generation of these vortices is due to the Kelvin-Helmholtz instability within the jet shear layer. The vortical structures existing in the jet shear layer are more prominent in the case of *Re* = 5,000, as clearly seen in the first two POD modes shown in Figure 10. However, vortical structures above the impingement plate seem to be the dominant features in the case of *Re* = 15,050, as shown in Figure 11.

The modes shown also confirm the findings of the LES study [8] which investigated the vortical structures and heat transfer in a round impinging jet for *H/D* = 2 and *Re* = 20,000. The interaction of large scale structures emanating from the jet shear layer with the wall-jet was found to lead to unsteady separation and the creation of distinct wall-attached vortices. The outward radial motion eventually breaks up these wall-attached vortices due to strong stretching resulting in their detachment and entrainment into the wall-jet. It was concluded that the breakup of the wall-attached vortices leads to the enhancement of the local momentum and heat transfer rates and potentially the appearance of a secondary Nusselt number peak [8]. In the current study, the wall-attached vortices form in the $r > 1$ region, for all modes and Reynolds numbers shown.

CONCLUSIONS

Time-Resolved PIV (TR-PIV) measurements were used to study the flow field resulting from a submerged water jet impinging normally on a smooth and flat surface. The jet issued from a long pipe that ensured fully developed turbulent flow conditions at the outlet. A semi-confined setting provided properly characterized flow boundary conditions. The Reynolds numbers based on jet mean exit velocity were 5,000, 10,030 and 15,050. The pipe-to-plate separation was 2*D*. Statistically averaged mean and RMS velocities are reported with a special emphasis on the near-wall region. For the studied small separation distances, *H/D* = 2, the core region of the axial jet is not influenced by the jet shear layer, resulting in stagnation region turbulence characteristics similar to the inflow conditions.

POD analysis of the TR-PIV data was used to gain insight into the most energetic coherent structures of the turbulent flow field. The snapshot POD was applied to an ensemble of 3,000 instantaneous PIV measurements that captured the flow field of the stagnation and wall-jet regions. Modes 1-10 were found to contain 39%, 41%, and 42% of the turbulent energy for *Re* = 5,000, 10,030 and 15,050, respectively. POD spatial distributions reveal that vortices along the impingement wall, outside of the stagnation region, were most prominent, especially in the *Re* = 15,050 case. The vortices forming in the jet shear layer were more prominent for *Re* = 5,000.

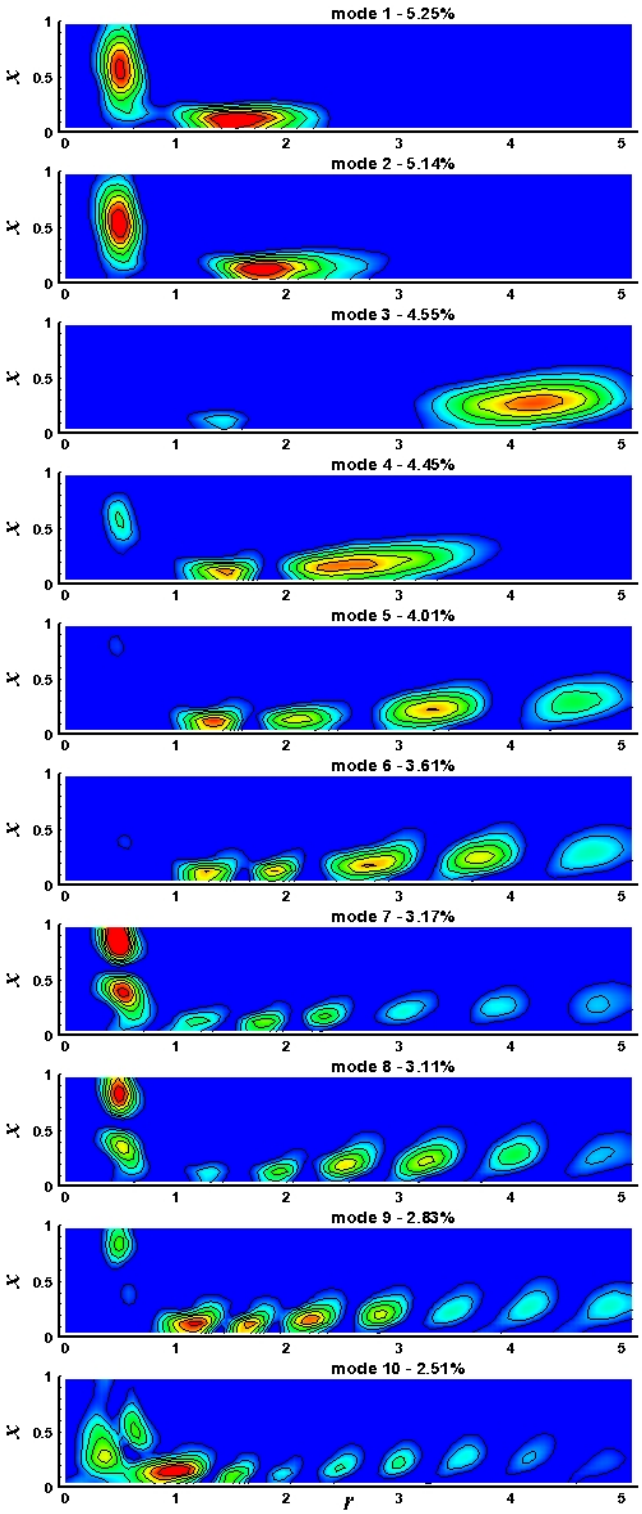

FIGURE 10. POD SPATIAL MODES 1-10 FOR RE = 5,000; CONTOURS OF VELOCITY MAGNITUDE

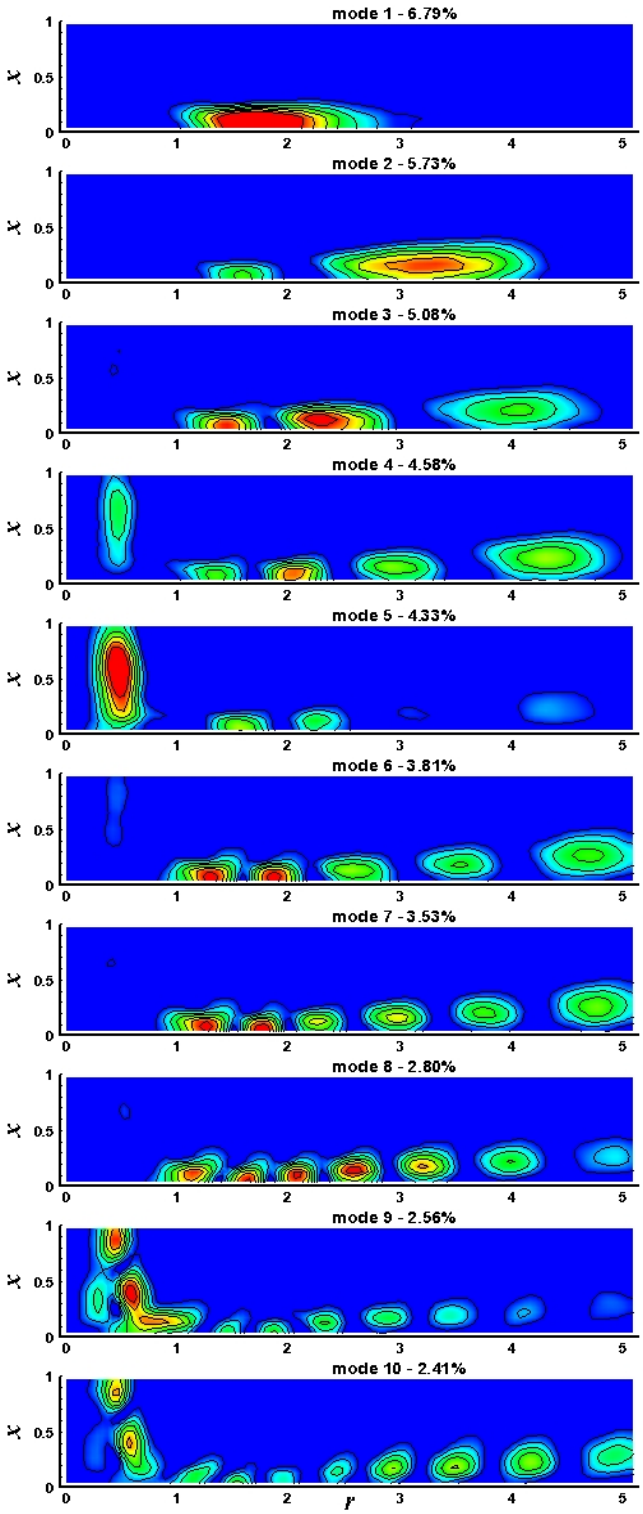

FIGURE 11. POD SPATIAL MODES 1-10 FOR RE=15,050; CONTOURS OF VELOCITY MAGNITUDE

ACKNOWLEDGEMENTS

The authors are grateful to Mr. Craig Goulbourne for his assistance with the experiment setup.

REFERENCES

[1] Martin, H, 1977. 'Heat and Mass Transfer Between Impinging Gas Jets and Solid Surfaces,' *Adv. Heat Transfer*, **13**, pp. 1-60.

[2] Downs, S. J., and James, E. H., 1987. 'Jet Impingement Heat Transfer – A Literature Survey,' ASME Paper No. 87-H-35, ASME, NY.

[3] Jambunathan, K., Lai, E., Moss, M. A., and Button, B. L., 1992. 'A Review of Heat Transfer Data for Single Circular Jet Impingement,' *Int. J. Heat and Fluid Flow*, **13**, pp. 106-115.

[4] Viskanta, R., 1993. 'Heat Transfer to Impinging Isothermal Gas and Flame Jets,' *Exp. Term. Fluid Sci.*, **6**, pp. 111-34.

[5] Polat, S., 1993. 'Heat and Mass Transfer in Impingement Drying,' *Drying Technol*., **11**, pp. 1147-1176.

[6] Webb, B., and Ma, C.-F., 1995. 'Single-Phase Liquid Jet Impingement Heat Transfer,' *Adv. Heat Transfer.*, **26**, pp. 105-134.

[7] Garimella, S. V., 1999. 'Heat Transfer and Flow Fields in Confined Jet Impingement,' Chapter 7, *Ann. Rev. Heat* Transfer, 11, pp. 413-494.

[8] Hadziabdic, M., and Hanjalic, K., 2008. 'Vortical Structures and Heat Transfer in a Round Impinging Jet,' *J. Fluid Mech.*, **596**, pp. 221-260.

[9] Hammad, K., and Milanovic, I.M., 2009. 'A POD Study of an Impinging Jet Flow Field,' ASME FEDSM09 conference, paper FEDSM09-78398, August 2-6, Vail, Colorado.

[10] Westergaard, C.H., Madsen, B.B., Marassi, M., and Tomasini, E.P., 2003. 'Accuracy of PIV Signals in Theory and Practice,' 5th International Symposium on Particle Image Velocimetry, Busan, Korea, September 22-24, Paper 3301.

[11] Meyer, K. E., Pedersen, J. M., Özcan, O., 2007, 'A Turbulent Jet in Crossflow Analyzed with Proper Orthogonal Decomposition,' *J. Fluid Mech.*, **583**, pp. 199-227.